PHOTONICS Research

Metal-to-ligand charge transfer chirality-based sensing of mercury ions

Xiongbin Wang,[1,2,†] Qiushi Wang,[3,†] Yulong Chen,[1,4,†] Jiagen Li,[5] Ruikun Pan,[3] Xing Cheng,[4] Kar Wei Ng,[1] Xi Zhu,[5] Tingchao He,[6,7] Jiaji Cheng,[3,8] Zikang Tang,[1,9] and Rui Chen[2,10]

[1]Institute of Applied Physics and Materials Engineering, University of Macau, Avenida da Universidade, Taipa, Macau 999078, China
[2]Department of Electrical and Electronic Engineering, Southern University of Science and Technology, Shenzhen 518055, China
[3]School of Materials Science and Engineering, Hubei University, Wuhan 430062, China
[4]Department of Materials Science and Engineering, Southern University of Science and Technology, Shenzhen 518055, China
[5]Shenzhen Institute of Artificial Intelligence and Robotics for Society (AIRS), Shenzhen 518172, China
[6]College of Physics and Optoelectronic Engineering, Shenzhen University, Shenzhen 518060, China
[7]e-mail: tche@szu.edu.cn
[8]e-mail: jiajicheng@hubu.edu.cn
[9]e-mail: zktang@um.edu.mo
[10]e-mail: chenr@sustech.edu.cn

Received 29 October 2020; revised 9 December 2020; accepted 13 December 2020; posted 15 December 2020 (Doc. ID 413592); published 26 January 2021

Chiral ligand conjugated transition metal oxide nanoparticles (NPs) are a promising platform for chiral recognition, biochemical sensing, and chiroptics. Herein, we present chirality-based strategy for effective sensing of mercury ions via ligand-induced chirality derived from metal-to-ligand charge transfer (MLCT) effects. The ligand competition effect between molybdenum and heavy metal ions such as mercury is designated to be essential for MLCT chirality. With this know-how, mercury ions, which have a larger stability constant (K_f) than molybdenum, can be selectively identified and quantified with a limit of detection (LOD) of 0.08 and 0.12 nmol/L for D-cysteine and L-cysteine (Cys) capped MoO_2 NPs. Such chiral chemical sensing nanosystems would be an ideal prototype for biochemical sensing with a significant impact on the field of biosensing, biological systems, and water research-based nanotoxicology. © 2021 Chinese Laser Press

https://doi.org/10.1364/PRJ.413592

1. INTRODUCTION

Ligand-induced chirality in semiconductor nanoparticles (NPs) has revolutionized the motif of inorganic material-based nanotechnology, because it timely opens the floodgate of these materials for promising applications in chiral recognitions and synthesis [1–5], bioimaging and display devices [6–15], and metamaterials in advanced optical devices [16–19] simply via interactions between the chiral ligands and achiral core [19–29]. Recently, ligand-induced chiral transition metal oxide ceramics have attracted tremendous interest not only due to their existing applications in optoelectronics [12,18,30] and biomedicine [31,32], but also their ability to provide incisive information on the metal-ligand interactions in terms of chiroptical activities. With both chemical linkage and coordination effects, electronic transitions between metal and ligands induce chiral responses in the visible region with a g-factor up to the order of 10^{-3}, which is 1 to 2 orders higher than that of traditional chiral ligand capped cadmium chalcogenide, where g-factor is defined as $\Delta\varepsilon/\varepsilon = \Delta A/A$, and ΔA is the absorbance difference between left- and right-handed circularly polarized light. Kotov and his coworkers [18], for instance, demonstrated that paramagnetic Co_3O_4 NPs with crystal lattice distortions caused by the chiral ligands exhibited both chiroptical activity in the visible range and intensive magnetic field-induced light modulation in the ultraviolet (UV) range, offering a versatile tool box for new technologies and knowledge at the nexus of chirality and magnetism. Moreover, their follow-up research work [33] showed the observation of induced chirality in $WO_{3-x} \cdot H_2O$ NPs via using proline (Pro) and aspartic acid (Asp) as surface ligands. The formed C-O-W linkages and weak coordination between amino groups and the core are found to be essential for the chiral metal-to-ligand charge transfer (MLCT) in the visible range and chiroplasmonic band in the near-infrared (NIR) region, respectively. To go further, the mentioned strong MLCT band is as well witnessed in our previous work [34] in a substoichiometric chiral Cys-capped MoO_{3-x} system with a large g-factor close to 7×10^{-3}, in which the MLCT band transition

is contributed by the transition from the metal-δ orbitals coupling with ligand-based π and π* orbitals. The g-factor originated from the MLCT band is about 100 times higher compared with the g-factor that comes from chiroplasmonic band transition in the NIR region [34]. Such strong chiroptical activity naturally motivates us to raise questions as this: is it possible to affect the MLCT chirality simply via the ligands, and can the materials be applied in the field of nanotechnology with specific applications such as chiral sensing?

To address the question, it is demonstrated herein chiral Cys reduced and capped MoO_2 NPs (L-/D-Cys-MoO_2) can serve as platform for ultralow concentration detection of mercury ions (Hg^{2+}) in water based on circular dichroism (CD) spectropolarimetry. The observed low limit of detection (LOD) and high selectivity on Hg^{2+} due to the large stability constant (log K_f) of Mo(cysteine)$_2$ highlight the potential of chiral MoO_2 NPs in the realm of chiral sensing and recognition. On the other hand, owing to the ligand competition effect, the surface ligand density of the chiral MoO_2 will be greatly impacted during Hg^{2+} introduction. The variation of ligand density linked to MLCT chirality with respect to CD response would unravel the chirogenesis and fundamental relations of ligand density versus MLCT chirality, providing intuitive experimental basis for studying the chiral electronic transitions in transition metal oxide ceramics.

2. EXPERIMENT SECTION

A. Materials

Molybdenum disulfide (MoS_2, 99.5%) powder and hydrogen peroxide (H_2O_2, GR, mass fraction 30% in H_2O) solution were purchased from Aladdin. L-Cys (98%), D-Cys (99%), and all soluble heavy metallic salts were obtained from Sigma-Aldrich. All chemicals were not purified for using as received. All heavy metal ion solution was prepared by adding the corresponding salt in water. The water that was used in all experiments had a resistivity higher than 18 $M\Omega \cdot cm^{-1}$.

B. Synthesis of Aqueous Molybdenum Trioxide Nanoparticles

The preparation of molybdenum trioxide MoO_3 NPs was reported previously [1,34]. First of all, 80 mg pristine MoS_2 powder was dissolved in 46.25 mL water in a beaker. Then, the dispersion was treated with sonication at room temperature. 3.75 mL H_2O_2 solution was added into the dispersion subsequently. The mixture was kept constantly stirred until the color turned from black to yellow. It would last about 20 h. Then, the dispersion was heated at about 70°C to remove excess H_2O_2. After about 1 h, the color of the dispersion would turn to transparent, which means the successful synthesis of MoO_3 NPs.

C. Preparation of Chiral MoO_2 Nanodots

The chiral MoO_2 nanodots were prepared according to the procedure given in the literature [1,31]. The as-prepared MoO_3 nanocrystals solution could be reduced and capped with the presence of chiral Cys molecules. In a typical process, 65 mg D-Cys was added into 1.5 mL MoO_3 solution that was obtained previously. Subsequently, the mixture was treated with sonication for 5 min. After that, the mixture was placed in the dark for one day to make sure that it could react sufficiently. The same treatment was carried out for obtaining D-Cys molecule capped MoO_2 nanodots.

D. Purification of Chiral Cys Capped MoO_2 Nanodots

After obtaining chiral molecule capped MoO_2 nanodots, the solution should be purified for further use. As in a typical process, the resulting solution was treated with centrifugation at 14,000 r/min for 20 min. Then, the supernatant was taken out from the centrifuge tube. The precipitate was dissolved in water. The mixture was centrifuged again at 6000 r/min for 10 min. After that, the supernatant was re-dissolved into another centrifuge tube. Finally, the mixture was again centrifuged at 5000 r/min for 5 min. The precipitate was dissolved in water for further use.

E. Characterizations

The UV-visible absorption measurement was carried out using a TU-1901 double-beam UV-Vis spectrophotometer (Beijing Purkine General Instrument Co., Ltd., China). For X-ray photoelectron spectroscopy (XPS) measurements, the samples were prepared by dropping the as-prepared solution on a silicon substrate, and the experiment was performed on a Thermo Scientific K-Alpha system. CD experiments were realized on a JASCO J-1500 CD spectrometer. The scan rate was 20 nm/min, and the data pitch was 0.1 nm. For all CD experiments, Milli-Q water with a quartz cuvette (0.1 cm optical path length from Hellma) was used. The transmission electron microscopy (TEM) pictures were captured by a Tecnai F30 microscope with operating voltage at 300 kV. A thermogravimetric analysis (TGA) experiment was conducted via Perkin Elmer STA 6000. The sample for measurement was dried under inert gas atmosphere. The measurement region is from 30 K to 800 K with a heating speed of 5°C per minute and 20°C per minute for the cooling process.

F. Stimulation Method

The nanocluster establishment and quantum chemical calculations were conducted with density functional theory (DFT). Ground state geometries were initiated and optimized at minimal energy state. The UV and CD simulated spectra were calculated at time-dependent density functional theory (TD-DFT) based on Gaussian 09 software. All the TD-DFT calculations were utilizing a B3LYP and LanL2DZ basis that was set for all the elements in simulation [35–37]. The small MoO_2 NPs capped with L- and D-Cys nanoclusters were constructed as a tetragonal crystal structure to form Mo_4O_8 neutral charge geometry to simulate the interactions between the molybdenum oxide cluster and chiral light.

G. Calculation of Ligand Density

The ligand density of NPs could be determined by the mass loss curve owing to the desorption and decomposition of the chemisorbed molecules [33,38]. First of all, the NPs for calculating were assumed to be spherical, and the diameter could be regarded as the average value of each NP obtained from the TEM image. The mass of an individual MoO_2 NP could be expressed as

$$m_{MoO_2} = \frac{\pi \rho D^3}{6},$$

where D is the average diameter of NPs and ρ is the density of the NP. The total amount of ligands (W_{cys}) and MoO_2 (W_{MoO_2}) in the system was obtained as

$$W_{cys} = W\varphi,$$

$$W_{MoO_2} = W - W_{cys},$$

where W is the total mass of sample for TGA measurement and φ is the mass fraction of Cys molecules on the NP surface. Then, the total number (N) for each sample was determined as

$$N = \frac{W_{MoO_2}}{m_{MoO_2}}.$$

Finally, the ligand density could be determined as

$$\text{Ligand density} = \frac{W_{cys}}{M_{cys}N} \cdot N_a \cdot \frac{1}{\pi D^2} = \frac{\varphi}{1-\varphi} \cdot \frac{\rho D}{6M_{cys}} \cdot N_a,$$

where N_a is the Avogadro constant and M_{cys} is the molecular weight of Cys. Here, D was 22.2 nm according to the TEM size distribution. ρ was assumed to be equal to the bulk MoO_2 density (6.47 g/cm^3). M_{cys} was equal to 121.15 g/cm^3 (CAS52-90-4).

3. RESULTS AND DISCUSSION

The representative illustrations of the chiral Cys-MoO_2 NPs and their application for Hg^{2+} sensing are shown in Fig. 1. Initially, transparent and colorless MoO_3 nanodots are fabricated via a two-dimensional MoS_2 layer through hydroperoxide oxidation. After that, aqueous chiral MoO_2 NPs using Cys molecules with D or L configuration serving as both the reducing agent and surface ligands are prepared according to a previous report (details are described in Section 2). With a valence state of +4, MoO_2 can be stable for more than one month in the open air. The surface Cys molecules could be exfoliated by Hg^{2+} easily owing to the higher stability constant of Hg(cysteine)$_2$ compared with Mo(cysteine)$_2$. The Cys molecules could again be adsorbed on the chiral Cys-MoO_2 surface, and the ligand was exfoliated by the introduced Hg^{2+}. A typical TEM image [Fig. 2(a)] shows that D-Cys-MoO_2 NPs are monodispersed with sphere morphology. The as-prepared D-Cys-MoO_2 NPs possess uniform size distribution with average diameter of 22.2 ± 0.3 nm [Fig. 2(b)].

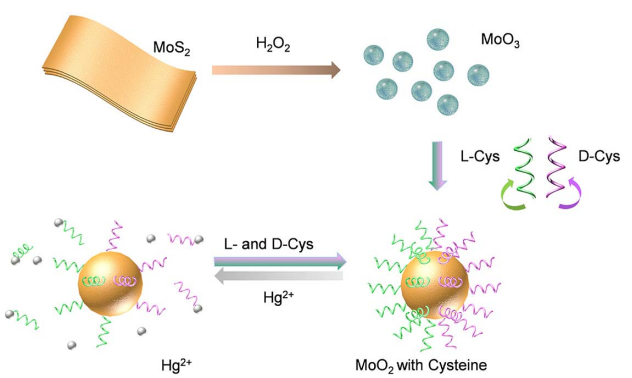

Fig. 1. Illustration of the synthesis process of chiral Cys-MoO_2 NPs and their application for Hg^{2+} sensing.

The chiroptical property of the MoO_3 NPs and Cys capped MoO_2 NPs is characterized by a CD spectrometer along with absorption measurement [Figs. 2(c) and 2(d)]. Without chiral ligands, the MoO_3 NPs are inactive in CD, while in the case of Cys reduced Cys-MoO_2 NPs, strong CD responses are recorded with opposite line shape depending on the enantiomer of chiral molecules used for the synthesis. Due to the MLCT effect, the observed CD signal is located in the visible range (350–650 nm) accompanied with merging UV-Vis absorption peaks within the same region (around 380 and 560 nm). The g-factors, which are calculated based on measured CD and absorption signal, are about 4.1×10^{-3} at 384 nm and 4×10^{-3} at 568 nm, respectively. The XPS survey scan is performed for both MoO_3 and D–Cys-MoO_2 samples. Figures 2(e) and 2(f) also plot the Mo 3d orbital spectra before and after reductive treatment under Cys molecules. Figure 2(e) shows two apparent peaks located at 233.15 and 236.35 eV, which correspond to the 3d5/2 and 3d3/2 orbitals for the Mo(VI), respectively. The result indicates that typical α-MoO_3 has been obtained. After the Cys reduction, the XPS peaks of Mo show obvious downshift, which move to 229 and 232.8 eV, respectively, as illustrated in Fig. 2(f) [34,39]. These binding energies are indexed as 3d5/2 and 3d3/2 orbitals for the Mo(IV). It confirms that excessive Cys could completely reduce the Mo in MoO_3 to the IV state without any intermediate states.

The observed MLCT chirality provides the possibility by using such chiral materials for heavy metal ion sensing especially Hg^{2+}. Note that the stability constant log K_f of Hg(cysteine)$_2$ is ca. 43.5, whereas those of Cd^{2+}, Zn^{2+}, Co^{2+}, Cu^{2+}, Pb^{2+}, and Mo^{4+} are ca. 17, 18, 16, 16, 12, and 21.5, respectively [40,41]. The stability constant of Hg^{2+} is the only one that is apparently larger than that of Mo^{4+}, which implies that Hg^{2+} is capable of removing thiolates chemisorbed on MoO_2 surface and decreasing the chiroptical properties of Cys-MoO_2 NPs via ligand competition. Based on this idea, chiral Cys-MoO_2 NPs can be a suitable candidate for Hg^{2+} sensing with better selectivity than traditional absorption or photoluminescence (PL)-based inorganic NPs. To probe the sensing capability, standard heavy metal ion solutions (Hg^{2+}, Cu^{2+}, etc.) were prepared with varied concentrations and added to as-synthesized chiral Cys-MoO_2 aqueous solutions for step-by-step CD measurements. Typical CD results for Hg^{2+} sensing are illustrated in Fig. 3.

Apparently, with the increase of Hg^{2+} concentration, the recorded CD and UV signals, no matter for L-Cys-MoO_2 or D-Cys-MoO_2 systems, decrease gradually [Figs. 3(a) and 3(b)], which indicates the chemical reactions are initiated between Hg^{2+} and Cys molecules that are located on the MoO_2 surface.

Considering that the absorption of the chiral system may change probably due to the volume increment or aggregations caused by introduction of Hg^{2+}, anisotropic g-factor is used here for evaluating the sensing performance to rule out the interference of concentration variation. At low Hg^{2+} concentration, the CD signal of the mixture is indistinguishable for both

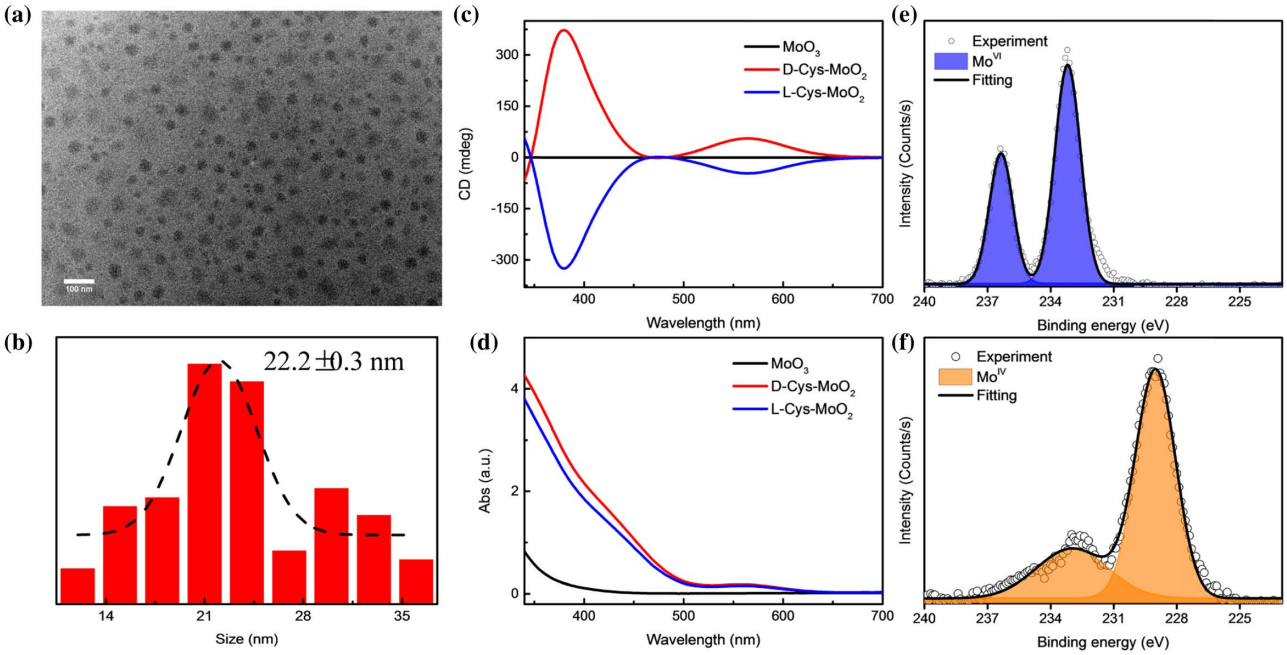

Fig. 2. (a) TEM image of D-Cys-MoO_2 NPs. The corresponding scale bar is 100 nm. (b) Histogram distribution of the diameter of NPs. Measurements of (c) circular dichroism spectrum and (d) absorption spectrum of MoO_3 (black line), L-Cys-MoO_2 (red line), and D-Cys-MoO_2 NPs (blue line). XPS spectra of (e) MoO_3 NPs and (f) D-Cys-MoO_2 NPs with deconvoluted molybdenum 3d peaks. The blue and orange peak areas are corresponding to the different valence states of Mo(VI) and Mo(IV), respectively.

D-Cys-MoO_2 and L-Cys-MoO_2 systems [as shown in Fig. 3(a)]. With the assistance of g-factor, the change of chiroptical property is better elucidated even when an ultrasmall amount (0.1 and 1 nM, 1 nM = 1 nmol/L) of Hg^{2+} is added to the chiral system as shown in Fig. 3(c) (black and red lines, for example). Moreover, Fig. 3(c) shows the relation of Hg^{2+} versus g-factor for the optical activity, suggesting a clear decreasing of g-factor values with the increase of Hg^{2+}. Figure 3(d) states the relationship between the increment of g-factor $\Delta g = g_0 - g$ at around 384 nm and Hg^{2+} concentration, where g and g_0 are the anisotropy factor without and with the presence of Hg^{2+} in solutions. The scatter plot and fitting curves of Δg show a growth tendency with the increase of Hg^{2+} concentration, which indicates that Cys molecules loaded at the surface of MoO_2 NPs had reacted with Hg^{2+} [Fig. 3(d)]. A linear increment of anisotropy factor at 384 nm versus the Hg^{2+} concentration ranging from 0.1 to 4 nM is established with correlation coefficients of 0.992 (for D-Cys-MoO_2 system) and 0.990 (for L-Cys-MoO_2 system). The LOD is determined to be 0.12 nM and 0.08 nM for L-Cys-MoO_2 and D-CysMoO_2, respectively. The LOD for Hg^{2+} detection is evaluated by $3\sigma/S$, where σ is the standard deviation of g-factor measured in the absence of

Table 1. Comparison of the Proposed Probe with Previously Reported Hg^{2+} Sensors Based on Different Methods[a]

Methods	System	Detection Range (nM)	LOD (nM)	Ref.
SERS	Au NPs/rGO/SiO_2/Si	0.1–6000	0.1	[42]
	Au TNAs/graphene/Au NPs	1–45,000	8.3	[43]
	4-MPY-Ag NPs	1–100	0.34	[44]
Absorption	DNA-Au NPs	0–5000	500	[45]
	N-T-Au NPs	50–250	0.8	[46]
	Hcy-SH	0–1000	72	[47]
PL	APBA-MoS_2	5–41,000	1.8	[48]
	N-doped-CNDs	0–300,000	80	[49]
	DNA-SWNTs	50–8000	14.5	[50]
Electrochemistry	HNTs-Fe_3O_4-MnO_2	2.5–750	1	[51]
	MSO-Au NPs	0–100	0.5	[52]
	DNA-Fc	1–2000	0.5	[53]
CD	DNA-Au NRs	0.25–50	0.15	[54]
	Ag-L-Cys NPs	0–1000	9	[55]
	D-Cys-MoO_2 NPs	0.1–30	0.08	This work
	L-Cys-MoO_2 NPs	0.1–30	0.12	This work

[a]rGO, reduced graphene oxide; TNAs, triangular nanoarrays; 4-MPY, 4-mercaptopyridine; N-T, thymine derivative; APBA, 3-aminobenzeneboronic acid; CNDs, carbon nanodots; SWNTs, single walled carbon nanotubes; HNTs, halloysite nanotubes; MSO, mercury-specific oligonucleotide; Fc, ferrocene; NRs, nanorods.

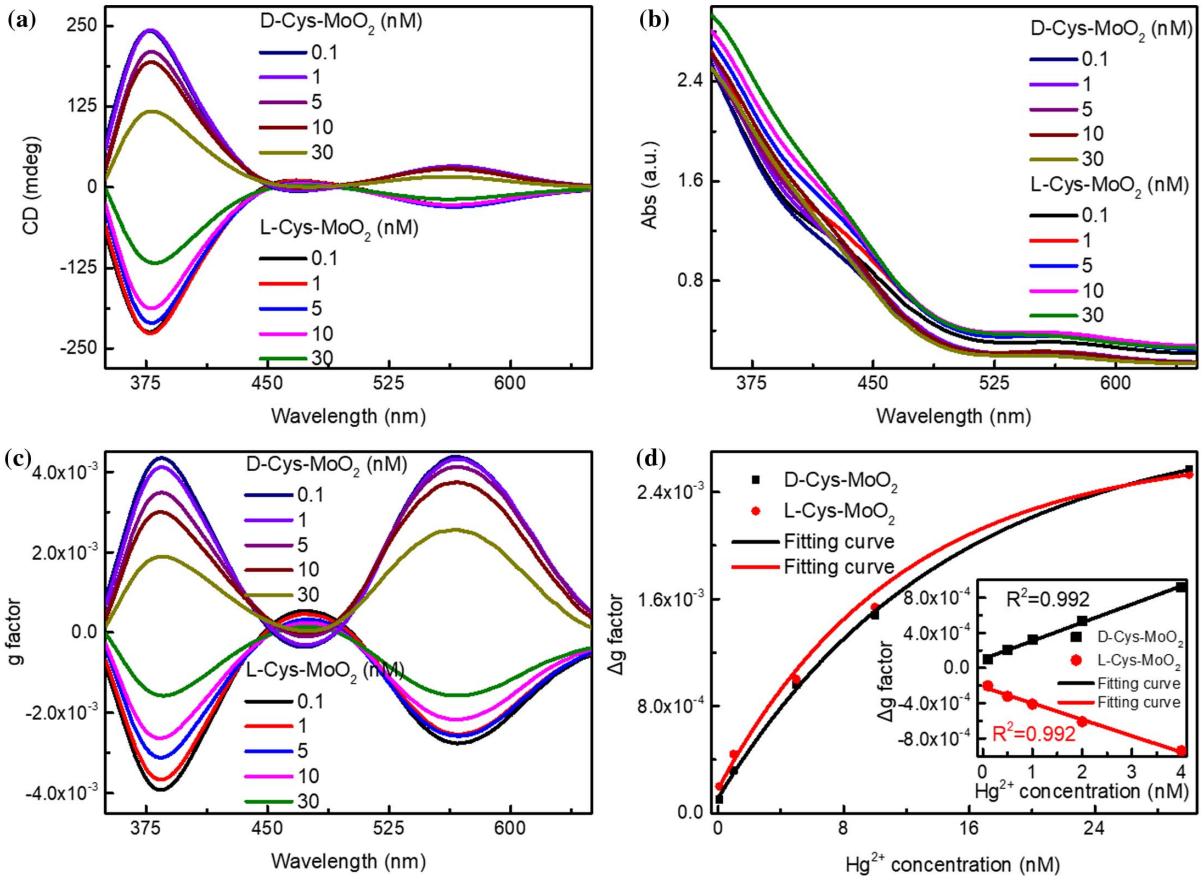

Fig. 3. Chiroptical sensing of Hg^{2+} using Cys-MoO_2 NPs. (a) CD and (b) absorption measurements for Hg^{2+} mixing with aqueous D-Cys-MoO_2 and L-Cys-MoO_2 NPs solution. The concentration of Hg^{2+} in the mixture varied from 0.1 nM to 30 nM. (c) Calculated *g*-factor curves of specimens in (a). (d) Differences of *g*-factor [values at 384 nm shown in (c)] versus Hg^{2+} concentration and corresponding fitting curve. The inset image is the calibration plot.

Hg^{2+}, and *S* is the slope of the calibrated plot. For comparison, the analytical characteristics of some Hg^{2+} sensors are summarized in Table 1. Obviously, the LOD of our sensing system is comparable to or better than the previously reported Hg^{2+} sensors based on surface-enhanced Raman scattering (SERS), absorption, PL, electrochemical and CD spectrum.

Based on previous researches by using fluorescent quantum dots for heavy metal ion sensing, two main mechanisms, namely the cation-exchange effect and ligand competition effect, are suggested to explain the quenching of chiroptical responses of Cys-MoO_2 systems discussed herein [56–58]. For the cation-exchange effect, Mo^{4+} will be replaced by Hg^{2+}, where there should be a clear shift in absorption spectra due to the formation of mercury-based compounds. Since there are no obvious shifts in both UV and CD spectra during Hg^{2+} addition [Figs. 3(a) and 3(b)], it can be confirmed that the cation-exchange effect is not involved in this case. As for the ligand competition effect, Hg^{2+} may exploit the thiol ligands from the MoO_2 surface leading to imperfection on the MoO_2 surface and decrement of chiral Cys molecules without spectral shifts. To verify the ligand competition effect, we particularly employ the TGA measurements for estimating the surface ligand packing density of L-Cys-MoO_2 NPs during the addition of Hg^{2+}. The plot of mass loss with temperature is shown in Fig. 4(a). The TGA curves exhibit three inflections of mass loss at about 230, 370, and 580°C, respectively, which correspond to different origins. The mass loss below 230°C could be regarded as the releasing of the physisorbed water and some pure Cys in the system. The second mass loss events could be attributed to desorption of Cys that is physisorbed on the surface of the NPs. The third mass loss comes from the decomposition of chemisorbed Cys. The estimated ligand density versus chiroptical responses caused by Hg^{2+} addition is summarized in Table 2. The mass loss of L-Cys is calculated to be 13.1%, 12.4%, 11.8%, 10.9%, and 10.1% for NPs with different

Table 2. Summary of Calculated Mass Loss and Ligand Density for L-Cys-MoO_2 NPs with Different Hg^{2+} Additions

Hg^{2+} Concentration (nM)	Mass Loss (%)	Ligand Density (nm^{-2})
0	13.1	17.96
0.1	12.4	16.86
1	11.8	15.94
5	11.4	15.33
10	10.9	14.57
30	10.1	13.38

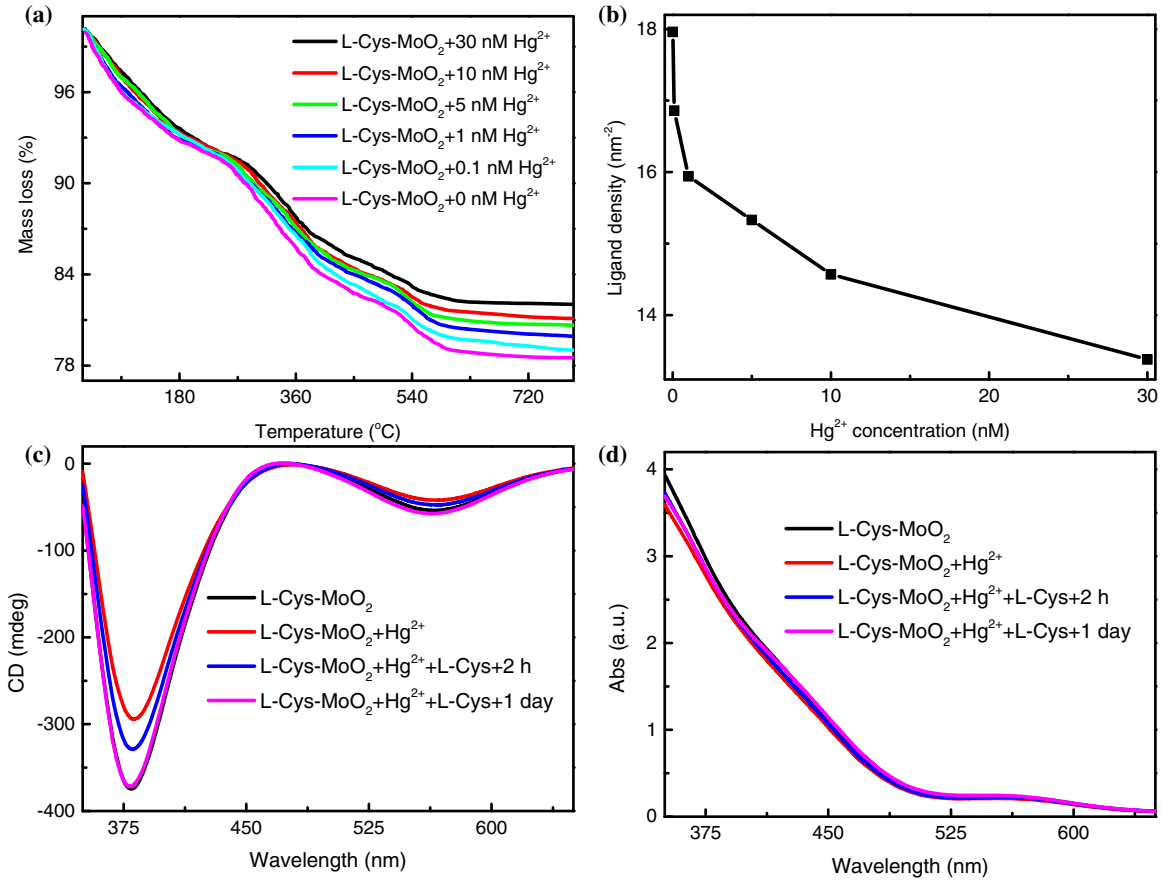

Fig. 4. (a) TGA curves of L-Cys-MoO_2 NPs with different amounts of mercury after dialysis. (b) Ligand density varies with mercury ion concentrations. (c) CD and (d) absorption spectra of pure L-Cys-MoO_2 NPs as well as L-Cys-MoO_2 mixing with Hg^{2+} (10 nM in the mixture) under different reaction times.

amounts of Hg^{2+}. The ligand density for these NPs could be estimated to be 17.96, 16.86, 15.94, 15.33, 14.57, and 13.38 nm^{-2}, respectively (for detail calculation, see Section 2). With the increase of Hg^{2+} concentration, an obvious decreasing of ligand density is witnessed [Fig. 4(b)]. Moreover, when chiral ligands were compensated after Hg^{2+} addition, the CD, UV, and *g*-factor spectra can be recovered to the original line shapes within one day incubation [Figs. 4(c) and 4(d)], indicating the ligand competition effect is the possible explanation for the MLCT chirality variation during Hg^{2+} addition.

To verify the relation between MLCT chirality and chiral ligand density on achiral core, simulations about orbital and molecular structure based on TD-DFT method are also implemented. Here, Mo_4O_8 nanoclusters are chosen as the smallest representative model that is anchored using different amounts of ligands with optimized geometry and energy level. For the chiral behavior transfer mechanism, the electronic state of the achiral NP core would hybridize with the chiral surface ligand, resulting in orbital wave function overlap. Figures 5(a)–5(d) show the calculated lowest unoccupied molecular orbitals (LUMOs) and highest occupied molecular orbitals (HOMOs) of the nanocluster with one and six capped D-Cys molecules, respectively. The HOMO shows strong wave function overlaps between the nanocluster and the Cys molecules. The HOMO-1 and HOMO-2 also show a semblable tendency for electronic state coupling. In contrast, the LUMO, LUMO + 1, and LUMO + 2 depict non-overlapping between the electronic state of the achiral core and chiral surface ligands. Therefore, the induction of chirality in the Mo_4O_8 nanocluster could be attributed to the orbital interactions. Figures 5(e) and 5(f) demonstrate the calculated CD and absorption spectra of different amounts of D-Cys capped Mo_4O_8 nanoclusters. Compared with the real metal oxide NPs, the simulated nanocluster is much smaller resulting in partially consistent CD spectra and absorption spectra with respect to our experiment results. The CD signal of the MLCT band around 380 nm exhibits a rising tendency while the absorption spectra are almost invariable with increasing Cys molecules functionalized onto the cluster, which is unanimous compared with our experimental results. With the increase of ligand quantity, a slight redshift could be overserved in the CD spectra that could be ascribed to the increased size of the nanocluster. Although the Cys capped metal oxide NPs are much more complicated than our established molecular model due to large degree of freedom, to some extent, our model could provide reference for the relationship between ligand density and chiroptical characteristics.

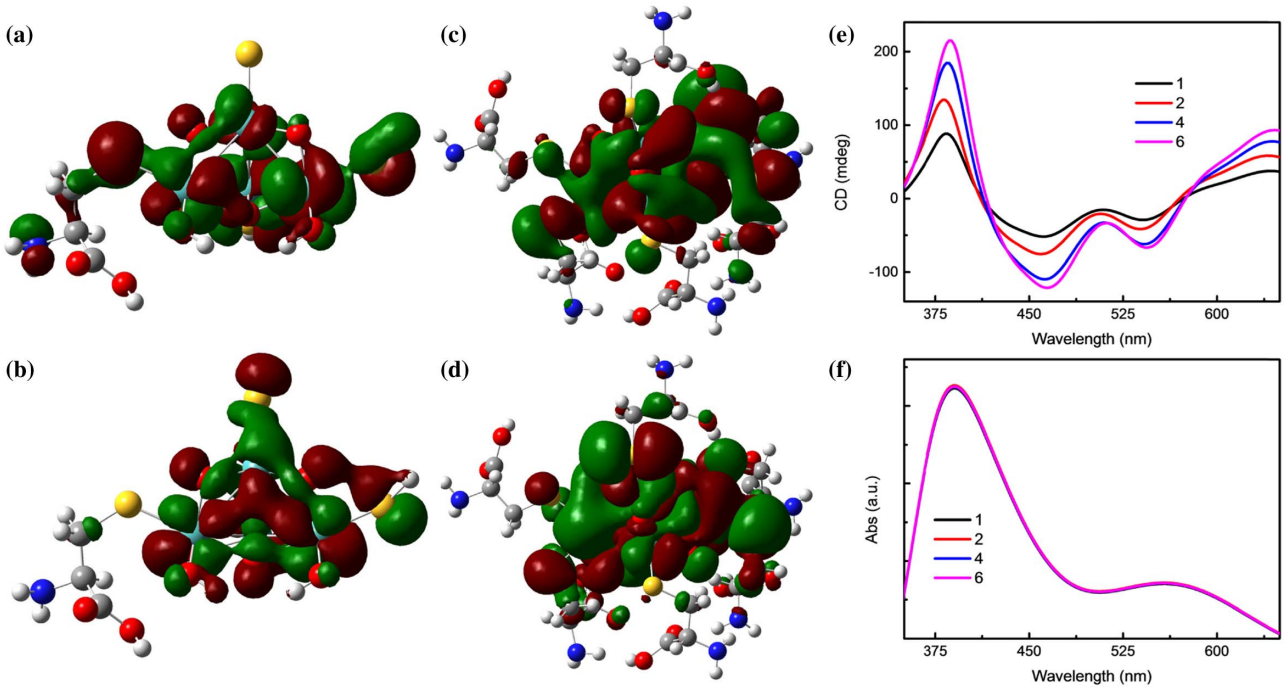

Fig. 5. TD-DFT simulation for different amounts of D-Cys capped Mo_4O_8 nanoclusters. Calculated frontier molecular orbital of (a), (c) HOMO and (b), (d) LUMO for one Cys molecule capped and six Cys molecule capped Mo_4O_8 nanoclusters. Calculated (e) CD spectra and (f) absorption spectra.

Further, with the know-how that heavy metal ions have a competition with the surface ligand, we examined such a phenomenon using different heavy metal ions to appreciate the selectivity of our chiral MoO_2 systems for Hg^{2+}. In particular, Zn^{2+}, Cd^{2+}, Pb^{2+}, Ag^{+}, and Cu^{2+} were applied to the same sensing setup followed by the standard treatments. The results are summarized in Fig. 6. As mentioned above, except for Hg^{2+}, the log K_f value for L-Cys-metal complexes of the heavy metals is basically smaller than that of Mo^{4+}. As a result, the chiral ligands on MoO_2 surface would be nearly unaffected, which exhibits inactive CD variation, demonstrating our chiral MoO_2 NP-based sensing platform has a good selectivity for Hg^{2+}. Therefore, chiral Cys-MoO_2 NPs can be a competitive chiral sensor for Hg^{2+} detection with high sensitivity and selectivity. The ligands on the Cys-MoO_2 surface play a critical role for not only stabilizing the NPs but also modulating MLCT chirality, providing the great potential of such nanosystems for green chemistry and water recycling.

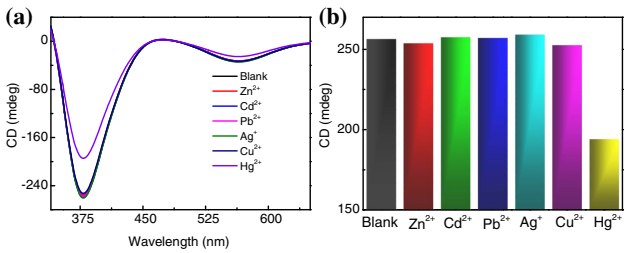

Fig. 6. Selectivity of D-Cys-MoO_2-based Hg^{2+} sensor. (a) CD spectra of D-Cys-MoO_2 solution mixed with different heavy metal ions: Zn^{2+}, Cd^{2+}, Pb^{2+}, Ag^{+}, Cu^{2+}, and Hg^{2+}. (b) CD signal at 384 nm of mixtures measured in (a). The concentrations of all metal ions are settled at 10 nM.

4. CONCLUSION

In summary, Cys-induced optically active MoO_2 NPs are synthesized and applied for Hg^{2+} detection with high precision. Due to the big stability constant of Hg(cysteine)$_2$, such a chiral sensing system is exceptionally sensitive to Hg^{2+} while inactive to other traditional heavy metal ions that coexist in waste water. Further CD observations, TGA analysis, and TD-DFT-based simulations confirm the ligand competition phenomenon between mercury and molybdenum, which unveils the underlying chirogenesis of MLCT chirality. Such transition metal oxide-based chiral NPs would be potential candidates for effective sensing of Hg^{2+} providing new horizons to the areas of biochemical sensing, chiroptics, and environmental remediation.

Funding. Science, Technology and Innovation Commission of Shenzhen Municipality (JCYJ20180305180553701, KQTD2015071710313656); Guangdong Basic and Applied Basic Research Foundation (2019A1515012094); Natural Science Foundation of Hubei Province (2020CFB200); Shenzhen Fundamental Research Foundation (JCYJ20180508162801893); National Natural Science Foundation of China (21805234, 22075240); Guangdong Introducing Innovative and Enterpreneurial Teams (2019ZT08L101); Shenzhen Institute of Artificial Intelligence and Robotics for Society (AIRS).

Disclosures. The authors declare no conflicts of interest.

†These authors contributed equally to this paper.

REFERENCES

1. J. Hao, Y. Li, X. Xu, F. Zhao, R. Pan, J. Li, H. Liu, K. Wang, J. Li, X. Zhu, M.-H. Delville, M. Zhang, T. He, and J. Cheng, "Metal-to-ligand charge transfer chirality sensing of D-glucose assisted with GOX-based enzymatic reaction," Adv. Mater. Technol. **5**, 2000138 (2020).
2. I. V. Martynenko, V. A. Kuznetsova, I. K. Litvinov, A. O. Orlova, V. G. Maslov, A. V. Fedorov, A. Dubavik, F. Purcell-Milton, Y. K. Gun'ko, and A. V. Baranov, "Enantioselective cellular uptake of chiral semiconductor nanocrystals," Nanotechnology **27**, 075102 (2016).
3. D. Meng, W. Ma, X. Wu, C. Xu, and H. Kuang, "DNA-driven two-layer core–satellite gold nanostructures for ultrasensitive microRNA detection in living cells," Small **16**, 2000003 (2020).
4. A. Kühnle, T. R. Linderoth, B. Hammer, and F. Besenbacher, "Chiral recognition in dimerization of adsorbed cysteine observed by scanning tunnelling microscopy," Nature **415**, 891–893 (2002).
5. S. Li, J. Liu, N. S. Ramesar, H. Heinz, L. Xu, C. Xu, and N. A. Kotov, "Single- and multi-component chiral supraparticles as modular enantioselective catalysts," Nat. Commun. **10**, 4826 (2019).
6. J. E. Govan, E. Jan, A. Querejeta, N. A. Kotov, and Y. K. Gun'Ko, "Chiral luminescent CdS nano-tetrapods," Chem. Commun. **46**, 6072–6074 (2010).
7. M. P. Moloney, Y. K. Gun'Ko, and J. M. Kelly, "Chiral highly luminescent CdS quantum dots," Chem. Commun. **38**, 3900–3902 (2007).
8. O. Cleary, F. Purcell-Milton, A. Vandekerckhove, and Y. K. Gun'Ko, "Chiral and luminescent TiO_2 nanoparticles," Adv. Opt. Mater. **5**, 1601000 (2017).
9. J. Ahn, E. Lee, J. Tan, W. Yang, B. Kim, and J. Moon, "A new class of chiral semiconductors: chiral-organic-molecule-incorporating organic–inorganic hybrid perovskites," Mater. Horiz. **4**, 851–856 (2017).
10. J. Hao, Y. Li, J. Miao, R. Liu, J. Li, H. Liu, Q. Wang, H. Liu, M.-H. Delville, T. He, K. Wang, X. Zhu, and J. Cheng, "Ligand-induced chirality in asymmetric CdSe/CdS nanostructures: a close look at chiral tadpoles," ACS Nano **14**, 10346–10358 (2020).
11. J. Cheng, J. Hao, H. Liu, J. Li, J. Li, X. Zhu, X. Lin, K. Wang, and T. He, "Optically active CdSe-dot/CdS-rod nanocrystals with induced chirality and circularly polarized luminescence," ACS Nano **12**, 5341–5350 (2018).
12. B. Zhao, H. Yu, K. Pan, Z. A. Tan, and J. Deng, "Multifarious chiral nanoarchitectures serving as handed-selective fluorescence filters for generating full-color circularly polarized luminescence," ACS Nano **14**, 3208–3218 (2020).
13. L. Wang, Y. Xue, M. Cui, Y. Huang, H. Xu, C. Qin, J. Yang, H. Dai, and M. Yuan, "A chiral reduced-dimension perovskite for an efficient flexible circularly polarized light photodetector," Angew. Chem. (Int. Ed.) **59**, 6442–6450 (2020).
14. C. Hao, X. Wu, M. Sun, H. Zhang, A. Yuan, L. Xu, C. Xu, and H. Kuang, "Chiral core–shell upconversion nanoparticle@MOF nanoassemblies for quantification and bioimaging of reactive oxygen species in vivo," J. Am. Chem. Soc. **141**, 19373–19378 (2019).
15. J. Yeom, P. P. G. Guimaraes, H. M. Ahn, B.-K. Jung, Q. Hu, K. McHugh, M. J. Mitchell, C.-O. Yun, R. Langer, and A. Jaklenec, "Chiral supraparticles for controllable nanomedicine," Adv. Mater. **32**, 1903878 (2020).
16. J. Govan and Y. K. Gun'ko, "Recent progress in chiral inorganic nanostructures," in *Nanoscience* (The Royal Society of Chemistry, 2016), Vol. **3**, pp. 1–30.
17. F. P. Milton, J. Govan, M. V. Mukhina, and Y. K. Gun'Ko, "The chiral nano-world: chiroptically active quantum nanostructures," Nanoscale Horiz. **1**, 14–26 (2015).
18. J. Yeom, U. S. Santos, M. Chekini, M. Cha, A. F. de Moura, and N. A. Kotov, "Chiromagnetic nanoparticles and gels," Science **359**, 309–314 (2018).
19. W. Ma, L. Xu, A. F. de Moura, X. Wu, H. Kuang, C. Xu, and N. A. Kotov, "Chiral inorganic nanostructures," Chem. Rev. **117**, 8041–8093 (2017).
20. W. A. Paiva-Marques, F. Reyes Gómez, O. N. Oliveira, and J. R. Mejía-Salazar, "Chiral plasmonics and their potential for point-of-care biosensing applications," Sensors **20**, 944 (2020).
21. J. Cheng, E. H. Hill, Y. Zheng, T. He, and Y. Liu, "Optically active plasmonic resonance in self-assembled nanostructures," Mater. Chem. Front. **2**, 662–678 (2018).
22. Y. Dong, Y. Zhang, X. Li, Y. Feng, H. Zhang, and J. Xu, "Chiral perovskite: chiral perovskites: promising materials toward next-generation optoelectronics," Small **15**, 1970209 (2019).
23. X. Gao, B. Han, X. Yang, and Z. Tang, "Perspective of chiral colloidal semiconductor nanocrystals: opportunity and challenge," J. Am. Chem. Soc. **141**, 13700–13707 (2019).
24. Y. Y. Lee, R. M. Kim, S. W. Im, M. Balamurugan, and K. T. Nam, "Plasmonic metamaterials for chiral sensing applications," Nanoscale **12**, 58–66 (2020).
25. A. Visheratina and N. A. Kotov, "Inorganic nanostructures with strong chiroptical activity," CCS Chem. **2**, 583–604 (2020).
26. Z. Wang, F. Cheng, T. Winsor, and Y. Liu, "Optical chiral metamaterials: a review of the fundamentals, fabrication methods and applications," Nanotechnology **27**, 412001 (2016).
27. R. Zhang, Y. Zhou, X. Yan, and K. Fan, "Advances in chiral nanozymes: a review," Microchim. Acta **186**, 782 (2019).
28. X. Zhao, S.-Q. Zang, and X. Chen, "Stereospecific interactions between chiral inorganic nanomaterials and biological systems," Chem. Soc. Rev. **49**, 2481–2503 (2020).
29. Y. Li, X. Wang, J. Miao, J. Li, X. Zhu, R. Chen, Z. Tang, R. Pan, T. He, and J. Cheng, "Chiral transition metal oxides: synthesis, chiral origins, and perspectives," Adv. Mater. **32**, 1905585 (2020).
30. J. Lv, D. Ding, X. Yang, K. Hou, X. Miao, D. Wang, B. Kou, L. Huang, and Z. Tang, "Biomimetic chiral photonic crystals," Angew. Chem. (Int. Ed.) **58**, 7783–7787 (2019).
31. Y. Li, Z. Miao, Z. Shang, Y. Cai, J. Cheng, and X. Xu, "A visible- and NIR-light responsive photothermal therapy agent by chirality-dependent MoO_{3-x} nanoparticles," Adv. Funct. Mater. **30**, 1906311 (2020).
32. S. Li, M. Sun, C. Hao, A. Qu, X. Wu, L. Xu, C. Xu, and H. Kuang, "Chiral Cu_xCo_yS nanoparticles under magnetic field and NIR light to eliminate senescent cells," Angew. Chem. (Int. Ed.) **59**, 13915–13922 (2020).
33. S. Jiang, M. Chekini, Z.-B. Qu, Y. Wang, A. Yeltik, Y. Liu, A. Kotlyar, T. Zhang, B. Li, H. V. Demir, and N. A. Kotov, "Chiral ceramic nanoparticles and peptide catalysis," J. Am. Chem. Soc. **139**, 13701–13712 (2017).
34. Y. Li, J. Cheng, J. Li, X. Zhu, T. He, R. Chen, and Z. Tang, "Tunable chiroptical properties from the plasmonic band to metal–ligand charge transfer band of cysteine-capped molybdenum oxide nanoparticles," Angew. Chem. (Int. Ed.) **57**, 10236–10240 (2018).
35. C. Lee, W. Yang, and R. G. Parr, "Development of the Colle-Salvetti correlation-energy formula into a functional of the electron density," Phys. Rev. B **37**, 785–789 (1988).
36. P. J. Hay and W. R. Wadt, "*Ab initio* effective core potentials for molecular calculations. Potentials for the transition metal atoms Sc to Hg," J. Chem. Phys. **82**, 270–283 (1985).
37. W. R. Wadt and P. J. Hay, "*Ab initio* effective core potentials for molecular calculations. Potentials for main group elements Na to Bi," J. Chem. Phys. **82**, 284–298 (1985).
38. B. M. Amoli, S. Gumfekar, A. Hu, Y. N. Zhou, and B. Zhao, "Thiocarboxylate functionalization of silver nanoparticles: effect of chain length on the electrical conductivity of nanoparticles and their polymer composites," J. Mater. Chem. **22**, 20048–20056 (2012).
39. Y. Sun, X. Hu, J. C. Yu, Q. Li, W. Luo, L. Yuan, W. Zhang, and Y. Huang, "Morphosynthesis of a hierarchical MoO_2 nanoarchitecture as a binder-free anode for lithium-ion batteries," Energy Environ. Sci. **4**, 2870–2877 (2011).
40. G. Berthon, "Critical evaluation of the stability constants of metal complexes of amino acids with polar side chains (technical report)," Pure Appl. Chem. **67**, 1117–1240 (1995).

41. D. Liu, W. Qu, W. Chen, W. Zhang, Z. Wang, and X. Jiang, "Highly sensitive, colorimetric detection of mercury(II) in aqueous media by quaternary ammonium group-capped gold nanoparticles at room temperature," Anal. Chem. **82**, 9606–9610 (2010).
42. X. Ding, L. Kong, J. Wang, F. Fang, D. Li, and J. Liu, "Highly sensitive SERS detection of Hg^{2+} ions in aqueous media using gold nanoparticles/graphene heterojunctions," ACS Appl. Mater. Interfaces **5**, 7072–7078 (2013).
43. X. Zhang, Z. Dai, S. Si, X. Zhang, W. Wu, H. Deng, F. Wang, X. Xiao, and C. Jiang, "Ultrasensitive SERS substrate integrated with uniform subnanometer scale 'hot spots' created by a graphene spacer for the detection of mercury ions," Small **13**, 1603347 (2017).
44. L. Chen, N. Qi, X. Wang, L. Chen, H. You, and J. Li, "Ultrasensitive surface-enhanced Raman scattering nanosensor for mercury ion detection based on functionalized silver nanoparticles," RSC Adv. **4**, 15055–15060 (2014).
45. X. Xu, J. Wang, K. Jiao, and X. Yang, "Colorimetric detection of mercury ion (Hg^{2+}) based on DNA oligonucleotides and unmodified gold nanoparticles sensing system with a tunable detection range," Biosens. Bioelectron. **24**, 3153–3158 (2009).
46. J. Du, Z. Wang, J. Fan, and X. Peng, "Gold nanoparticle-based colorimetric detection of mercury ion via coordination chemistry," Sens. Actuators B **212**, 481–486 (2015).
47. Y. Wang, M. Gao, C. Liao, F. Yu, and L. Chen, "A sulfydryl-based near-infrared ratiometic fluorescent probe for assessment of acute/chronic mercury exposure via associated determination of superoxide anion and mercury ion in cells and *in vivo*," Sens. Actuators B **301**, 127038 (2019).
48. X. Guo, J. Huang, Y. Wei, Q. Zeng, and L. Wang, "Fast and selective detection of mercury ions in environmental water by paper-based fluorescent sensor using boronic acid functionalized MoS_2 quantum dots," J. Hazard. Mater. **381**, 120969 (2020).
49. L. Wang, B. Li, F. Xu, X. Shi, D. Feng, D. Wei, Y. Li, Y. Feng, Y. Wang, D. Jia, and Y. Zhou, "High-yield synthesis of strong photoluminescent N-doped carbon nanodots derived from hydrosoluble chitosan for mercury ion sensing via smartphone APP," Biosens. Bioelectron. **79**, 1–8 (2016).
50. L. Zhang, T. Li, B. Li, J. Li, and E. Wang, "Carbon nanotube–DNA hybrid fluorescent sensor for sensitive and selective detection of mercury(II) ion," Chem. Commun. **46**, 1476–1478 (2010).
51. M. Fayazi, M. A. Taher, D. Afzali, and A. Mostafavi, "Fe_3O_4 and MnO_2 assembled on halloysite nanotubes: a highly efficient solid-phase extractant for electrochemical detection of mercury(II) ions," Sens. Actuators B **228**, 1–9 (2016).
52. Z. Zhu, Y. Su, J. Li, D. Li, J. Zhang, S. Song, Y. Zhao, G. Li, and C. Fan, "Highly sensitive electrochemical sensor for mercury(II) ions by using a mercury-specific oligonucleotide probe and gold nanoparticle-based amplification," Anal. Chem. **81**, 7660–7666 (2009).
53. S.-J. Liu, H.-G. Nie, J.-H. Jiang, G.-L. Shen, and R.-Q. Yu, "Electrochemical sensor for mercury(II) based on conformational switch mediated by interstrand cooperative coordination," Anal. Chem. **81**, 5724–5730 (2009).
54. Y. Zhu, L. Xu, W. Ma, Z. Xu, H. Kuang, L. Wang, and C. Xu, "A one-step homogeneous plasmonic circular dichroism detection of aqueous mercury ions using nucleic acid functionalized gold nanorods," Chem. Commun. **48**, 11889–11891 (2012).
55. J. Nan and X.-P. Yan, "Facile fabrication of chiral hybrid organic–inorganic nanomaterial with large optical activity for selective and sensitive detection of trace Hg^{2+}," Chem. Commun. **46**, 4396–4398 (2010).
56. S. Kacmaz, K. Ertekin, D. Mercan, O. Oter, E. Cetinkaya, and E. Celik, "An ultra sensitive fluorescent nanosensor for detection of ionic copper," Spectrochim. Acta A **135**, 551–559 (2015).
57. X. Wang, Y. Lv, and X. Hou, "A potential visual fluorescence probe for ultratrace arsenic (III) detection by using glutathione-capped CdTe quantum dots," Talanta **84**, 382–386 (2011).
58. T. Gong, J. Liu, X. Liu, J. Liu, J. Xiang, and Y. Wu, "A sensitive and selective sensing platform based on CdTe QDs in the presence of L-cysteine for detection of silver, mercury and copper ions in water and various drinks," Food Chem. **213**, 306–312 (2016).